Supplementary Figures

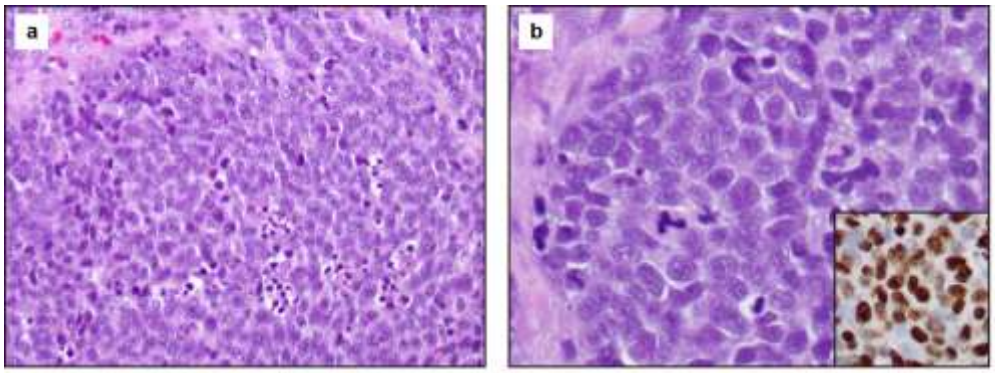

Supplementary Figure 1: Microscopic characteristics of the small cell carcinoma of the index responder. **(A)** The tumor culled from two distinct surgeries was identical in histology and consisted of solid sheets of tumor cells separated by delicate fibrovascular stroma. **(B)** Tumor nuclei were uniform and round to oval with nuclear overlapping, evenly distributed chromatin, and no prominent nucleoli. The cytoplasm was scant and abundant mitotic figures and apoptotic bodies were present. The proliferation marker Ki-67 (Mib-1) was expressed in the vast majority of tumor cells (inset).

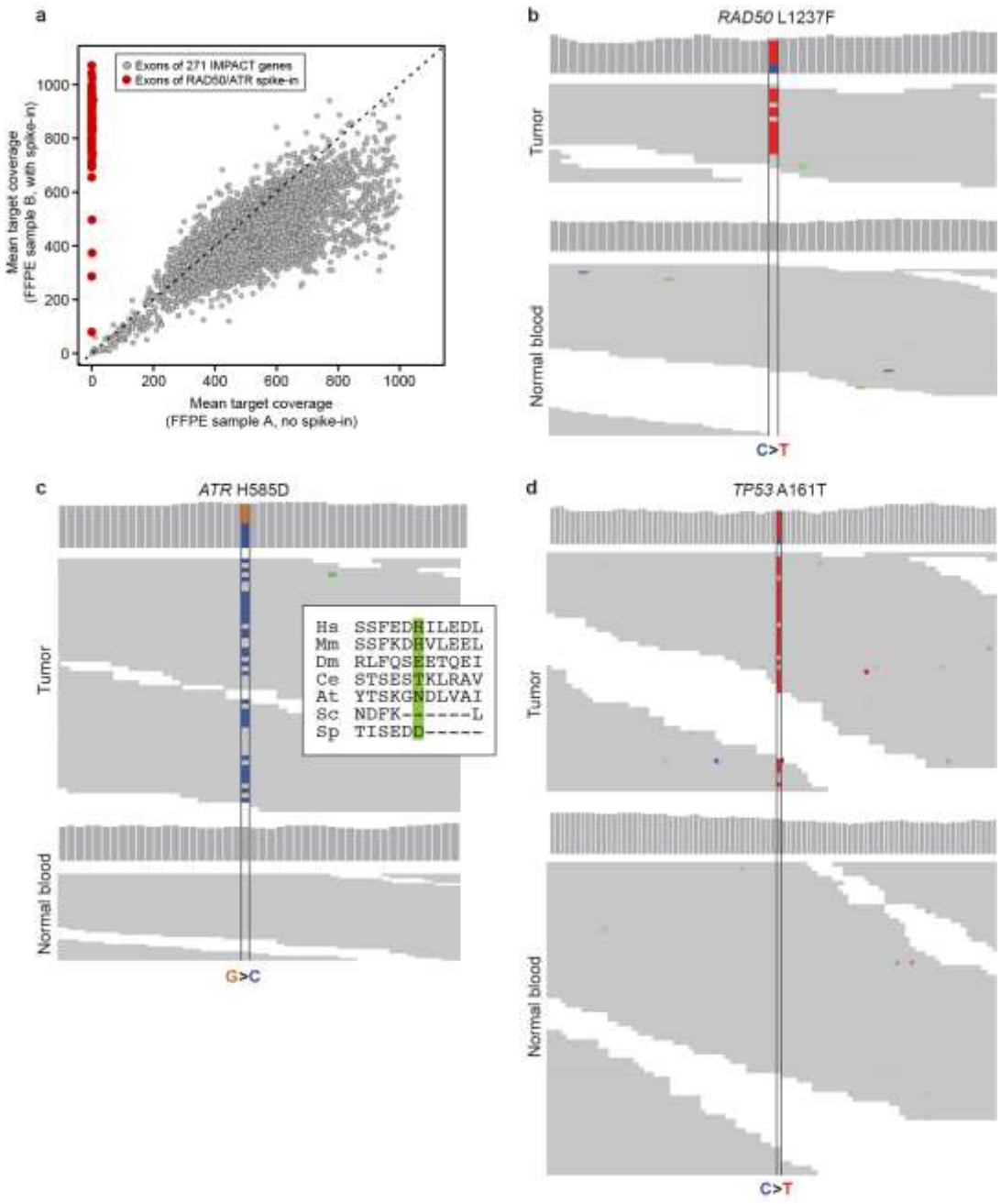

Supplementary Figure 2: Effectiveness of spike-in approach for acquiring coverage with IMPACT and key mutational data. **(A)** Shown here is the mean target coverage for exons in the 279 genes of the current IMPACT design and those exons of *RAD50* and *ATR* covered by the spiked-in oligonucleotides in a single representative normal FFPE sample from a small cell carcinoma patient in an independent cohort (y-axis) compared to a similar normal sample run at the same time but lacking the spike-in. This indicates high coverage was achieved across the exons of the spike-in. **(B-D)** Identified mutations in the checkpoint control and DNA repair machinery where aligned reads from whole-genome sequencing of the tumor and matched normal DNA reflect either the mutant or reference allele in each of **(B)** RAD50 L1237F, **(C)** ATR H585D (inset is multiple sequence alignment indicating low sequence conservation; abbreviations as in main text figure 2C), and **(D)** TP53 A161T.

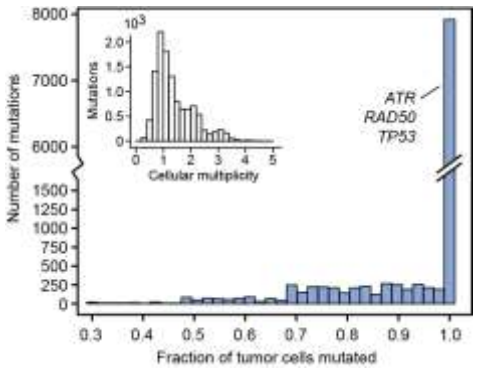

Supplementary Figure 3: The clonal composition of somatic mutations detected in the index responder's tumor. The distribution of the fraction of tumor cells mutated for the point mutations and indels identified in the whole genome sequence is shown. While >95% of all mutations were clonal (100% of tumor cells), individual genes of interest are indicated, including several subclonal mutations (*FAT1* and *XPO1*). Inset, the same distribution represented as the cellular multiplicity of each mutation.

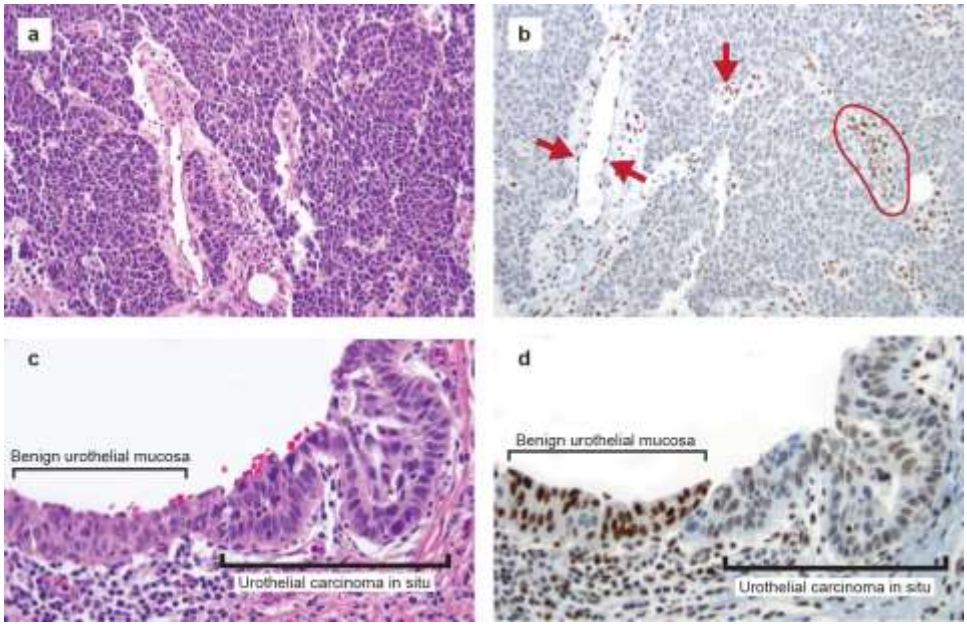

Supplementary Figure 4: RAD50 immunohistochemistry (IHC). **(A)** Invasive carcinoma with neuroendocrine features from the recurrent tumor of the index responder prior to trial enrollment. **(B)** RAD50 IHC indicates a marked reduction of RAD50 expression in tumor cells compared to normal adjacent endothelial cells (arrows) and tumor-infiltrating lymphocytes (circled). **(C)** Section of ureter showing benign urothelial mucosa adjacent to in situ urothelial carcinoma. **(D)** Reduced RAD50 expression (IHC as in panel B) is apparent in cells of urothelial carcinoma in situ compared to the adjacent benign urothelial mucosa.

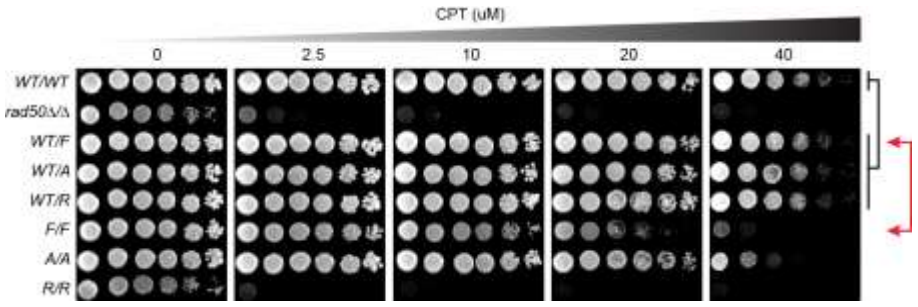

Supplementary Figure 5: *rad50*^{L1240} mutants are not dominant negative. There was no observable dominant negative phenotype among *rad50*^{L1240} mutants in CPT survival. Five-fold serial dilutions of heterozygote or homozygote diploid cells as indicated (250,000 cells per spot to 80 cells per spot) were spotted on YPD plates without or with the indicated concentrations of camptothecin (CPT). Plates were incubated at 30 degrees for 2 days. The comparison of interest is highlighted in red. WT, wildtype; F, *rad50*^{L1240F}; A, *rad50*^{L1240A}; R, *rad50*^{L1240R}.

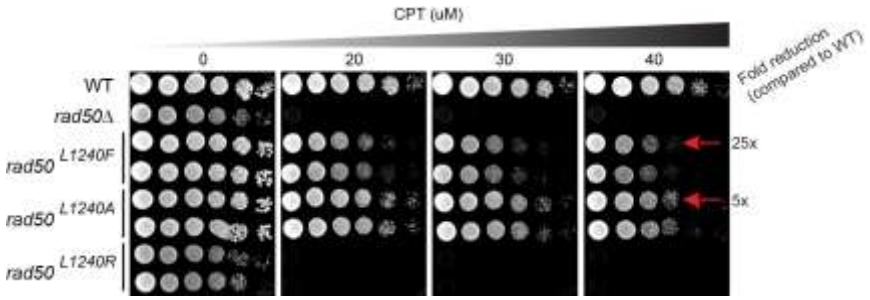

Supplementary Figure 6: Survival of *rad50*-L1240 mutants. Here, the survival of various *rad50*^{L1240} mutants in the presence of high concentrations of camptothecin (CPT) is shown. Five-fold serial dilutions of haploid cells (250,000 cells per spot to 80 cells per spot) were spotted on YPD plates with or without indicated concentrations of CPT. Plates were photographed after 2 days of incubation at 30 degrees. Independent duplicate spores of the *rad50*^{L1240} mutants were assessed. The comparison of interest is highlighted in red, indicating the fold reduction observed (left).

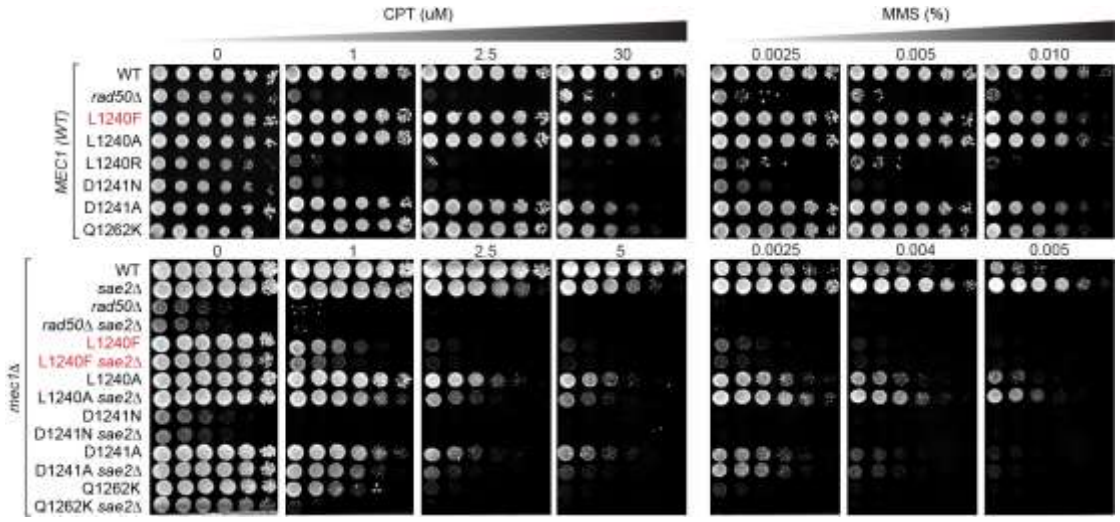

Supplementary Figure 7: The ATM ortholog Tel1 is defective in *rad50*^{L1240F} mutants. Illustrating TM pathway function (see Supplementary Note) as in figure 3B of the main text but at additional concentrations, the sensitivity of mec1Δ cells to the DNA damaging agent methyl methanesulfonate (MMS) is markedly reduced by Sae2 deletion (*mec1*Δ and *mec1*Δ *sae2*Δ mutants respectively). In *rad50*^{L1240F} *mec1*Δ *sae2*Δ mutants, MMS sensitivity is equal to that of *rad50*^{L1240F} *mec1*Δ alone, indicating that the TM pathway is inactivated by the *rad50*^{L1240F} mutation, and therefore the ATM ortholog Tel1 is defective. Also visible here, *rad50*$^{L1240F/A}$ is slightly more sensitive than are wildtype cells to MMS at higher doses, which is in agreement with their partial CPT sensitivity. The other D-loop mutation *rad50*^{D1241N} is dead at the lowest 1uM dose of CPT and cannot be rescued by Sae2 deletion in *mec1*Δ cells (0.0025% MMS plate).

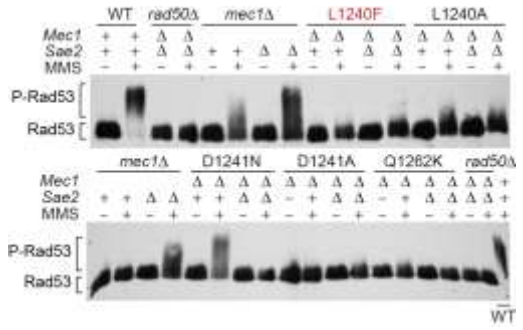

Supplementary Figure 8: RAD50 mutations impair ATM signaling. Here, Rad53 phosphorylation levels are significantly reduced in all *rad50* mutants with the exception of the residual levels in the innocuous *rad50*^{L1240A} mutant. The loss of Sae2 in *mec1*Δ cells, while stimulating Rad53 phosphorylation as expected in Rad50 wildtype cells, which are uniquely dependent on ATM ortholog Tel1 (see Supplementary Note), cannot rescue the *rad50*-mutant signaling defect in any of the mutants tested.

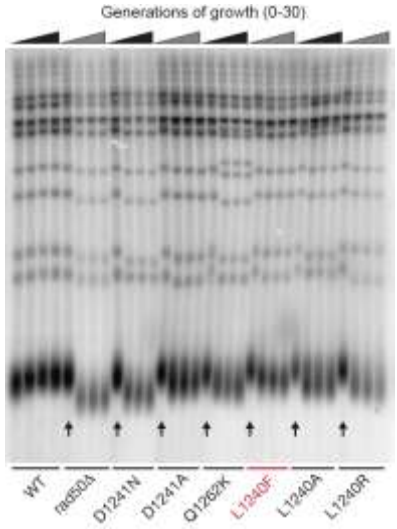

Supplementary Figure 9: Telomere shortening in Tel1-defective rad50-mutant cells. Telomere lengths, the maintenance of which are governed in part by Tel1 kinase activity, are shorter in all haploid *rad50* mutants compared to those in diploid cells of the indicated mutant/WT, confirming the Tel1 defect. Arrows indicate diploid mutant/WT (as indicated, lanes 5, 9, 13, 17, 21, 25, and 29) at generation 0, indicating the presence of wildtype telomere length. At right of each diploid are haploid spores at 10, 20, and 30 generations of growth.

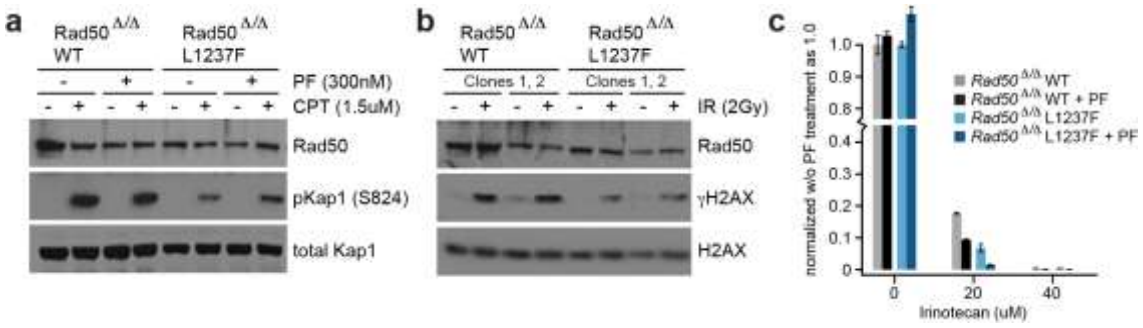

Supplementary Figure 10: Impaired ATM signaling and associated phenotypes in Rad50 L1237F-mutant mammalian cells. **(A)** Rad50 Null over null MEFs engineered to express either wildtype Rad50 or Rad50 L1237F were treated with either the Chk1 inhibitor PF-477736 (PF), camptothecin (CPT), or their combination after which phosphorylation of the ATM substrate Kap1 was assessed. As indicated, reduced phosphorylation of Kap1 at Ser824, an ATM-dependent site, was apparent upon co-treatment in Rad50 L1237 cells. This confirms the RAD50 L1237F-mediated ATM signaling defect persists in mammalian cells. Moreover, while the affect is modest, these MEF data likely underestimate the severity of the signaling defect because they were selected to express normal amounts of Rad50 L1237F, whereas RAD50 IHC in the tumor of the index patient (Supplementary Fig. 4) indicated reduced protein levels. **(B)** MEFs expressing only Rad50 L1237F have reduced γH2AX formation following irradiation, indicating ATM activation is compromised. **(C)** While reduced colony formation was apparent upon irinotecan treatment regardless of Rad50 status and decreased further (<2-fold) in combination with Chk1 inhibitor PF-477736 (PF), a significant further decrease (~5-fold) was apparent in Rad50 L1237F mutant cells. Experiments performed in triplicate, error bars are stdev.